Stripe Patterns in Wind Forecasts Induced by Physics-Dynamics

2 Coupling on a Staggered Grid in CMA-GFS 3.0

- 3 Jiong Chen^{1,2,3}, Yong Su^{1,2,3}, Zhe Li^{1,2,3}, Zhanshan Ma^{1,2,3}, Xueshun Shen^{1,2,3}
- 4 ¹State Key Laboratory of Severe Weather Meteorological Science and Technology, Beijing, 10081,
- 5 China

24

1

- 6 ²CMA Earth System Modeling and Prediction Centre (CEMC), Beijing, 10081, China
- 7 ³Key Laboratory of Earth System Modeling and Prediction, China Meteorological Administration,
- 8 Beijing, 10081, China
- 9 Correspondence to: Jiong Chen (cjiong@cma.gov.cn) and Xueshun Shen (shenxs@cma.gov.cn)
- 10 **Abstract.** An unphysical stripe pattern is identified in low-level wind field in China Meteorological
- 11 Administration Global Forecast System (CMA-GFS), characterized by meridional stripes in u-
- 12 component and zonal stripes in *v*-component. This stripe noise is primarily confined to the planetary
- boundary layer over land. The structural mismatch between static field variations and the observed
- 14 $2\Delta x$ noise amplitude suggests that locally forced mechanisms from surface inhomogeneity alone
- 15 cannot explain the wind stripe patterns. Meanwhile, pure dynamical core simulations exhibit no
- 16 <u>such noise, confirming that the dynamical core itself does not generate these patterns The absence</u>
- 17 of noise in both surface static fields and pure dynamic-core solutions proves that neither the
- 18 <u>dynamical core nor physical parameterizations alone can produce wind stripe patterns</u>. These results
- 19 suggest that staggered-grid mismatch in physics-dynamics coupling is likely the primary
- 20 mechanism. Idealized two-dimensional experiments demonstrate that combining one-dimensional
- 21 dynamic-core advection and physics-based vertical diffusion on a staggered grid generates $2\Delta x$ -
- 22 wavelength spurious waves when surface friction is non-uniform. One-dimensional linear wave
- 23 analysis further confirms that staggered-grid coupling between dynamic advection and
- analysis further confirms that staggered-grid coupling between dynamic advection and
- validate that eliminating grid mismatch in physics-dynamics coupling removes this stripe noise.

inhomogeneous damping forcing induces dispersion errors in wave solutions. Sensitivity tests

- 26 These findings collectively indicate that while staggered grids benefit the dynamic core's numerical
- 27 stability and accuracy, their inherent grid mismatch with physics parameterizations requires

specialized coupling strategies to avoid spurious noise. Potential solutions to remedy this issue are discussed.

1. Introduction

28

29

30

31

32

33

34

35 36

37

38 39

40

41 42

43 44

45

46

47 48

49

50

51

52

53 54

55

56

The wind field, as a fundamental state variable in atmospheric dynamics, governs not only the accuracy of circulation forecasts but also controls the spatiotemporal distributions of temperature, humidity, aerosols, and cloud microphysical properties through advection processes. Numerical weather prediction (NWP) systems simulate three-dimensional wind field evolution through numerical integration of atmospheric governing equations with multi-scale physical parameterizations. The momentum equations describe wind field evolution through three key forces: the pressure gradient force, Coriolis force, and nonlinear advection terms. The numerical discretization of advection terms is particularly important as it directly affects solution stability (Durran, 2010). Parameterized physical processes at subgrid scale significantly influence wind field predictions. Surface stress not only exerts substantial control over the wind intensity in both the near-surface and planetary boundary layers (PBL) through turbulent momentum transport (Blackadar, 1957; Stull, 1988), but also significantly influences the location of the surface westerlies and upper-level jets in the midlatitudes (Robinson, 1997; Chen et al., 2007). When flow encounters subgrid-scale orography, it excites gravity waves that propagate vertically, altering large-scale winds through momentum flux divergence (McFarlane, 1987; Kim et al., 2003; Kim and Doyle, 2005). Mesoscale topographic blocking and turbulent form drag modify low-level wind fields, which in turn affect global circulation patterns (Beljaars et al., 2004; Sandu et al., 2016). In addition to dynamics and physical processes, the consistency of dynamic-physics coupling is equally critical for overall model performance (Bauer et al., 2015; Gross et al., 2016; 2018). In NWP model, numerical noise typically stems from non-physical high-frequency oscillations induced by dynamical process discretization (Wurtele, 1961; Arakawa, 1966; Mesinger & Arakawa, 1976). Additionally, spatial grid mismatch in physics-dynamic coupling can generate computational noise (Chen et al., 2020). While consistent spatial grids between dynamical and physical processes are theoretically preferable for seamless coupling, practical implementations often employ differing horizontal and vertical grid configurations. For vertical discretization, two conventional grid arrangements are employed: (1) the Lorenz grid (Lorenz, 1960), collocating thermodynamic

(temperature/moisture) and dynamic (wind) variables at half-levels, and (2) the Charney-Phillips (CP) grid (Charney & Phillips, 1957), staggering wind variables at half-levels while thermodynamic variables at full-levels. Chen et al. (2017) demonstrated that Lorenz-grid physics coupled with CP-grid dynamics generates non-physical computational modes in PBL scheme solutions. Chen et al. (2020) confirmed that unified grid coupling significantly improves the stratocumulus representation and overall forecast skill while eliminating this spurious noise. These findings underscore that dynamic-physical coupling inconsistencies not only introduce numerical noise but also substantially degrade model performance.

In global models, physical processes are typically computed in single columns, independent of horizontal grid configuration. Thus, horizontally distributed noise cannot originate from physical parameterizations if the underlying static physical data is noise-free. In two-dimensional rectangular

57

58

59

60

61

62

63

64

65 66

67

68 69

70

71 72

73

74

75

76

77

78

79

80 81

82 83

84

85

86

parameterizations if the underlying static physical data is noise-free. In two-dimensional rectangular grids, horizontal grid configurations are categorized into non-staggered (A-grid) and staggered (B grid to E grid) types, distinguished by their arrangement of wind components (u, v) and mass variables (height z or pressure p) (Arakawa and Lamb, 1977). Among these, the Arakawa C-grid – where mass variables are collocated at grid centers while velocity components are staggered at cell interfaces - exhibits optimal accuracy when the grid spacing resolves scales smaller than the Rossby radius of deformation (Batteen & Han, 1981; Xu & Lin, 1993; Randall, 1994). This superiority stems from its inherent conservation properties and reduced numerical dispersion in simulating geostrophic adjustment processes (Arakawa and Lamb, 1977; Randall, 1994). The Arakawa-C grid has been widely implemented as a preferred discretization framework in structured-grid NWP systems, including the Weather Research and Forecasting (WRF) Model's Advanced Research core (Skamarock et al., 2008) and operational systems such as the UK Met Office Unified Model (Walters et al., 2017), the NOAA Global Forecast System (GFS) (Sela, 2010), the Environment and Climate Change Canada (ECCC) Global Environmental Multiscale (GEM) model (Côté et al., 1998), and the China Meteorological Administration's (CMA) operational GRAPES system (Chen et al., 2008). Figure 1 illustrates the wind field distribution on an Arakawa C-grid, where the physicsparameterized winds are located at the central mass points while the dynamically computed winds are staggered at the cell interfaces. This inherent wind field grid mismatch is typically handled via two-step interpolation during physics-dynamics coupling. However, as demonstrated by Chen et al. (2020), the grid inconsistency during physics-dynamics coupling introduces spurious computational 87 noise.

88

89 90

91

92

93

94 95

96

97

98

99

100

101 102

103

104

105

106

107

108

109

110

111

112113

114

High-order horizontal diffusion (Xue, 2000) and filters (Shapiro, 1970, 1975; Raymond and Garder, 1988) are standard techniques for suppressing high-frequency computational noise in NWP models. These approaches were successfully implemented in the GRAPES model and effectively mitigated small-scale noise (Wang et al., 2008). Compared to CMA-GFS 2.4 (originally GRAPES_GFS V2.4), the new CMA-GFS 3.0 has removed fourth-order horizontal diffusion to improve small-scale system simulation capabilities (Shen et al., 2023). Following the upgrade to CMA-GFS 3.0, stripe patterns became evident in the low-level wind fields—an issue absent in previous versions. This study systematically investigates the underlying causes of these stripe patterns in CMA-GFS 3.0, particularly examining physics-dynamics coupling mismatches as the probable source. Section 2 details physics-dynamics coupling scheme on a staggered grid for the wind field prediction in CMA-GFS 3.0 and characterizes the observed horizontal wind noise patterns. Section 3 identifies noise sources via idealized experiments and analytical wave solutions, revealing fundamental discretization constraints in physics-dynamics coupling. Section 4 designs sensitivity experiments to verify the origin of horizontal wind noise in CMA-GFS 3.0, conclusively attributing it to physics-dynamics coupling mismatches. Conclusions and discussions are presented in Section 5.

2. The wind prediction in the PBL in CMA GFS

2.1 Model description and physics-dynamic coupling in wind prediction

The CMA-GFS (formerly known as GRAPES_GFS) was developed based on a two-time-level semi-implicit semi-Lagrangian (SISL) non-hydrostatic dynamic core. Its development began in 2007, and the system became operational in late 2015 (Shen et al., 2020). The model employs a horizontal Arakawa C-grid on a regular latitude-longitude grid, combined with a vertical CP grid using a height-based terrain-following coordinate system (Chen et al., 2008).

Physics package includes the Rapid Radiative Transfer Model for GCMs (RRTMG) for longwave and shortwave radiation (Pincus et al. 2003; Morcrette et al. 2008), the double-moment microphysics and an explicit prognostic cloud cover scheme (Ma et al. 2018), the common land

model (CoLM) (Dai et al. 2003), the subgrid-scale orographic (SSO) scheme including gravity wave drag (GWD) (Chen et al. 2016) and turbulence orographic form drag (TOFD) (Beljaar et al., 2004), the new Simplified Arakawa Schubert (NSAS) convection, and the new medium-range forecast (NMRF) for vertical diffusion (Han and Pan 2011). The implementation of vertical diffusion and cloud physics schemes on the CP grid eliminated computational noise induced by physics-dynamics coupling mismatches, leading to significant improvements in stratocumulus cloud simulations and overall forecast skill scores (Chen et al., 2020).

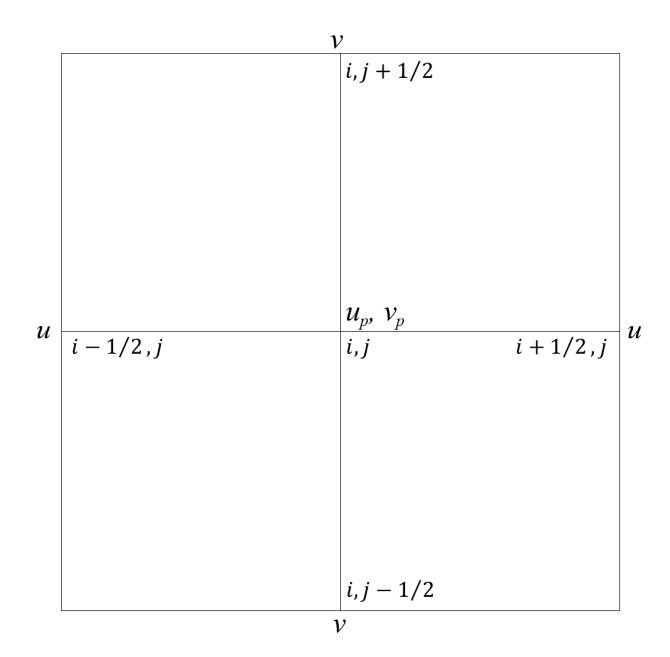


Figure 1. Wind configuration in Arakawa C grid; the subscript 'p' denotes the physics grid points

In CMA-GFS's dynamical core, horizontal winds $u_{i\pm\frac{1}{2}j}$ and $v_{i,j\pm\frac{1}{2}}$ are staggered at cell interfaces, while physics-parameterized winds u_p and v_p are collocated at mass center (Figure 1). In our coupling scheme, linear interpolation bridges the grid mismatch for physics-dynamics coupling:

$$\begin{cases} P(u_{i,j}) = P\left(\frac{u_{i-\frac{1}{2},j} + u_{i+\frac{1}{2},j}}{2}\right) \\ P(v_{i,j}) = P\left(\frac{v_{i,j-\frac{1}{2}} + v_{i,j+\frac{1}{2}}}{2}\right) \end{cases}$$
(1)

- 128 where P denotes the physics parameterization operator. When feeding physics tendencies back to
- the dynamical core, the coupling follows:

$$\begin{cases}
\Delta u_{i+\frac{1}{2},j}^{P} = \frac{1}{2} [P(u_{i,j}) + P(u_{i+1,j})] \Delta t \\
\Delta v_{i,j+\frac{1}{2}}^{P} = \frac{1}{2} [P(v_{i,j}) + P(v_{i,j+1})] \Delta t
\end{cases}$$
(2)

- where ΔV^P denotes the physics-induced wind increment to be fed back to the dynamic core.
- 131 However, such interpolation-based coupling schemes often fail to mitigate computational noise
- induced by physics-dynamics grid mismatches (Chen et al. 2020).
- As theoretically anticipated, lower-level winds of CMA-GFS 3.0 exhibit distinct stripe patterns.
- 134 We therefore systematically investigate these anomalies in detail, first characterizing their
- spatiotemporal structures, and then evaluating potential links to physics-dynamics coupling
- 136 mechanisms.

2.2 Spatiotemporal distribution of wind forecast noise: a case study

- In this case study—hereafter referred to as Exp_Ctrl—we utilize CMA-GFS 3.0 with a
- horizontal resolution of 0.25° (approximately 25 km at the equator) and 87 vertical levels extending
- up to 1 hPa. The simulation spans from 1200 UTC 1 July 2021, initialized with European Centre
- 141 for Medium-Range Weather Forecasts (ECMWF) ERA5 reanalysis data (Hersbach et al., 2020; data
- available at https://cds.climate.copernicus.eu/datasets/). Hourly forecast fields are saved directly on
- the model's Arakawa C-grid at model levels throughout the 5-day simulation.
- 144 Global distribution of the wind field noise reveals pronounced land-sea contrasts, with
- 145 predominant stripe patterns over land while relatively smooth over oceans. Figure 2 displays the 18-
- hour forecast (valid at 0600 UTC) of near-surface winds at the lowest model level over South Asia
- 147 (88-113°E, 5-34°N), a region encompassing both land and ocean. Distinct stripe patterns dominate
- 148 the wind field over land areas, where the u-component displays meridional stripes and the v-
- component exhibits zonal stripes. With the model's 0.25° resolution, these structures are clearly
- resolved with a wavelength of 0.5° ($2\Delta x$), demonstrating characteristic $2\Delta x$ wave properties.

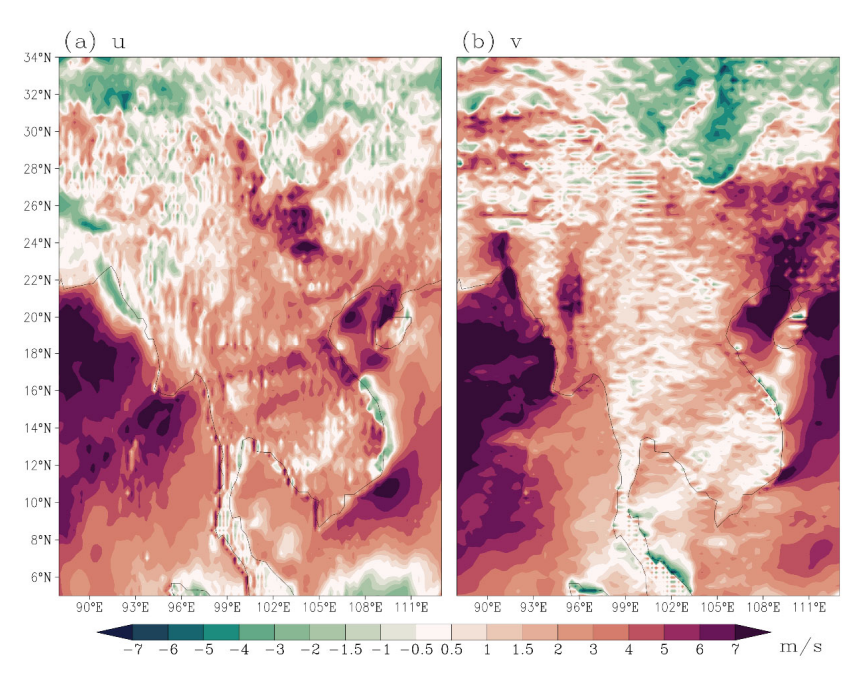


Figure 2. 18-hour forecast of (a) u- and (b) v- components at the lowest model level from CMA-GFS 3.0

Figure 3 displays vertical cross-sections of u- and v- components along 30°N and 100°E, respectively, for the region shown in Fig. 2. Pronounced $2\Delta x$ wave patterns are evident throughout the PBL in both components, whereas the wind field becomes markedly smoother in the free atmosphere above the PBL. The strongest $2\Delta x$ signatures are concentrated in the bottom of the PBL.

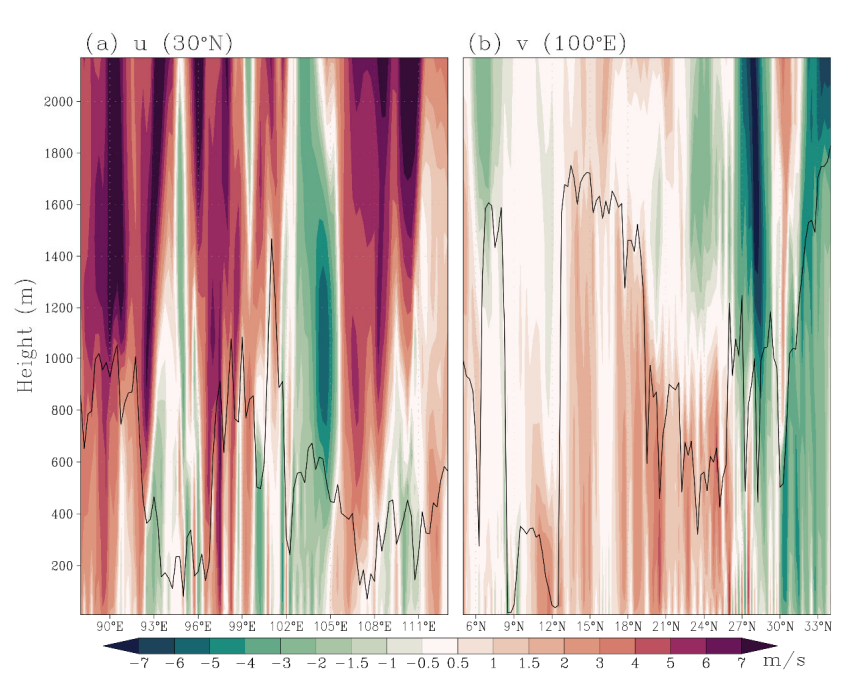


Figure 3 Vertical distribution of 18-hour forecasted winds: (a) u-component along 30°N; (b) v-component along 100°E. Black solid lines denote the PBL height.

 Figure 4 presents the 120-hour (5-day) evolution of surface-layer u- and v- components along the zonal and meridional transects shown in Fig. 3. The $2\Delta x$ oscillations exhibit continuous presence throughout the period. Their amplitude shows strong diurnal variations but no systematic growth with forecast days, suggesting that this noise is unlikely to directly induce model instability while exhibiting diurnal amplitude modulation. This persistent noise pattern shows daytime intensification and nighttime weakening, suggests a potential linkage to the inherent diurnal cycle of the development of PBL.

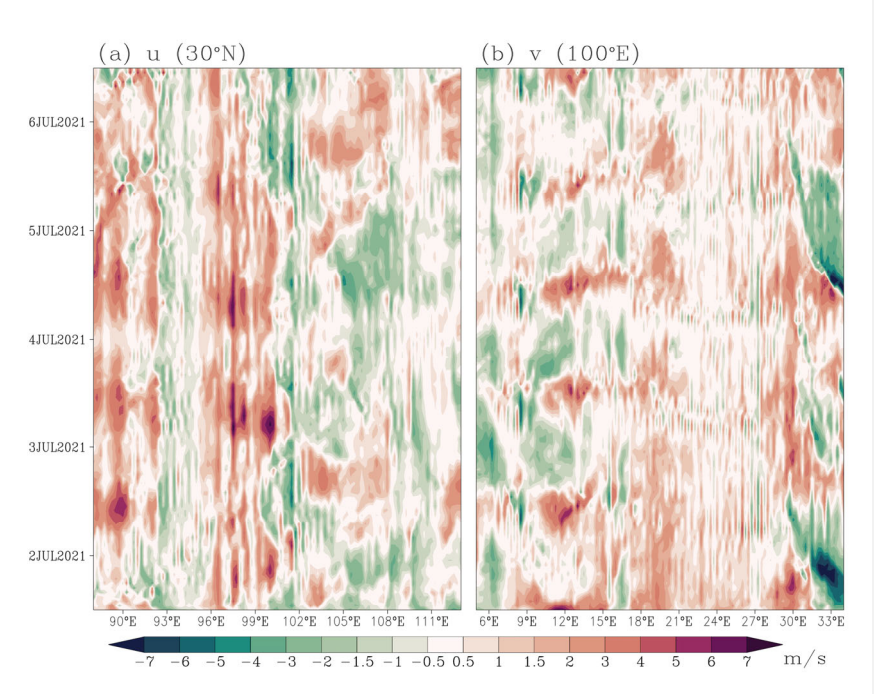


Figure 4. Temporal evolution of winds at the lowest model level (0-120 hours): (a) u-component along 30°N, (b) v-component along 100°E.

The vertical structure of low-level winds and their diurnal variations in the surface layer imply a connection between the stripe patterns and momentum-related physical processes, particularly turbulent transport within the PBL. However, the single-column design of physical schemes permits PBL diffusion to affect such horizontal wind noise solely via surface friction forcing. In the following section, we systematically examine the mechanisms for these $2\Delta x$ stripe patterns.

3. Tracing the cause of wind stripes predicted in CMA-GFS 3.0

3.1 Examination of associated surface static fields

 The surface static fields directly governing surface friction in the wind field are surface inhomogeneity descriptors, principally characterized by subgrid orographic variability and aerodynamic roughness length. Figure 5 displays the spatial distributions of subgrid orography standard deviation and momentum roughness length across the domain shown in Fig. 2.

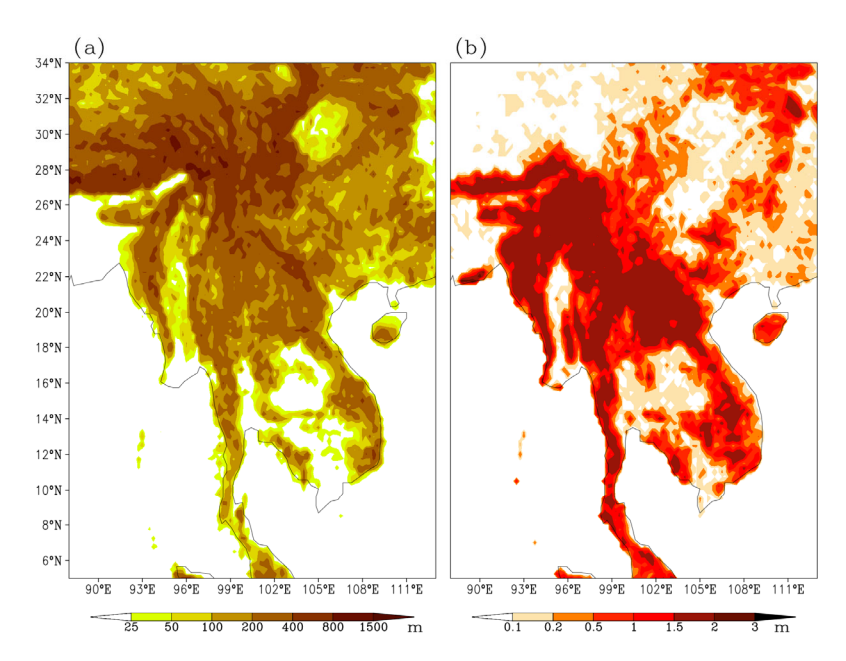


Figure 5. Horizontal distributions of (a) Standard deviation of sub-grid orography; (b) Roughness length over the study region (domain same as Fig. 2).

The distributions of the two static fields in Fig. 5 differ markedly from the wind stripe patterns in Fig. 2, indicating that surface parameter inhomogeneity is not the direct origin of the stripe noise The complete absence of $2\Delta x$ noise in both static fields shown in Figure 5 contrasts sharply with the wind stripes observed in Fig. 2, definitively excluding surface parameters inhomogeneity as direct contributors to the noise generation. However, visual comparison with Fig. 2 demonstrates a distinct spatial correspondence between the stripe noise locations and the surface roughness distribution: the $2\Delta x$ noise patterns predominantly occur over areas with higher roughness, while remaining absent over smooth surfaces. The Andaman Islands (11–13°N, 93°E), located between the Bay of Bengal and the Andaman Sea, generate localized surface inhomogeneity in this predominantly oceanic region. Consistent with this inhomogeneity, Fig. 2 exhibits obvious meridional stripes in the u- component precisely over this archipelago. These observations imply that although the surface inhomogeneity parameters themselves exhibit no stripe patterns—and thus cannot directly produce the wind stripes through physical processes—the spatial organization of $2\Delta x$ noise systematically correlates with surface inhomogeneity.

3.2 Dynamical Core Tests: Noise Assessment in Physics-off simulation

Section 3.1 demonstrated that the surface-friction-related static fields lack horizontal noise patterns (Fig. 5), definitively excluding surface-mediated physical processes—which are computed in single columns—as possible sources of the observed $2\Delta x$ wind stripes. We now evaluate the dynamical core's potential contribution through a physics-free simulation using identical configuration described in section 2.2. Figure 6 displays 18-hour forecasts of near-surface u- and v-components over the same domain as in Fig. 2. The absence of surface friction yields stronger winds compared to the default physics-on simulation (Fig. 2), and more critically, the wind fields exhibit smooth distributions completely free of $2\Delta x$ stripes. This definitive evidence excludes the dynamical core as the source of the observed low-level wind noise.

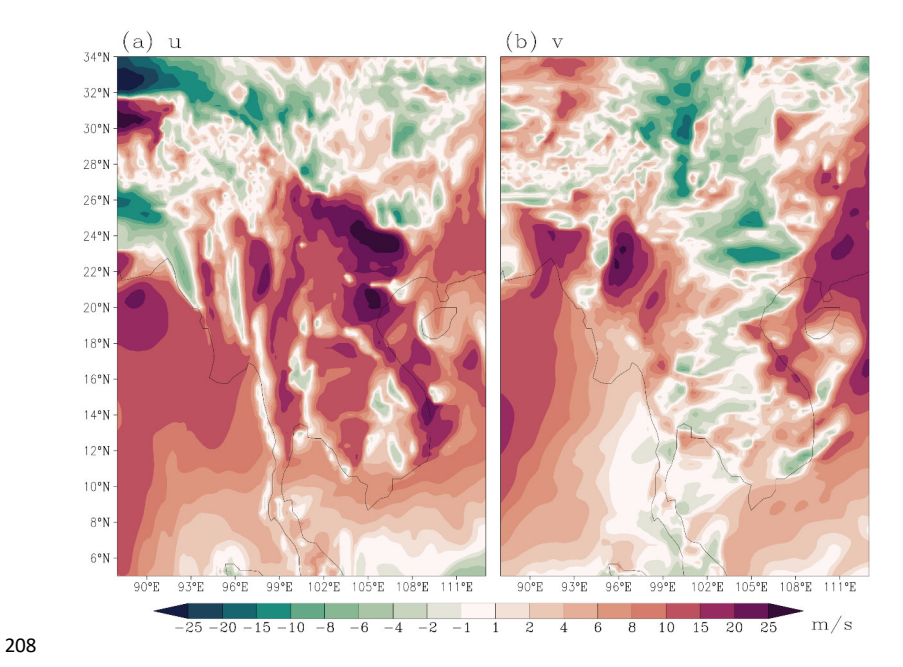


Figure 6. Same as Fig. 2, but for the physics-off experiment

Having definitively excluded both the dynamical core and physical parameterizations as direct sources of these horizontal noise patterns, the residual evidence points to the physics-dynamics coupling interface as the sole remaining candidate. As schematized in Fig. 1, CMA-GFS employs staggered grids between physics and dynamics components, requiring linear interpolation for wind

- field coupling. This inherent grid mismatch is now the most probable mechanism generating the observed $2\Delta x$ stripe noise. We proceed with idealized experiments and theoretical analysis to examine whether the grid mismatch between physics and dynamics could induce the computational noise.
- 218 3.3 Two-dimensional idealized test
- The governing equation for the idealized simulation combining one-dimensional horizontal advection with vertical diffusion is

$$\frac{\partial u}{\partial t} + u \frac{\partial u}{\partial x} = -\frac{\partial \overline{u'w'}}{\partial z} \tag{3}$$

- where u is flow speed and $\overline{u'w'}$ the turbulent vertical momentum flux. In Equation (3)(3), the nonlinear term $u\frac{\partial u}{\partial x}$ represents the dynamical advection process, while the right-hand side $-\frac{\partial \overline{u'w'}}{\partial z}$
- 223 represents the physical forcing process, specifically parameterized turbulent vertical transport. The
- 224 momentum flux can be expressed as:

$$\overline{u'w'} = -K\frac{\partial u}{\partial z} \tag{4}$$

where K(z) is the height dependent eddy diffusivity given by:

$$\begin{cases} K(z) = \frac{0.5z\left(1 - \frac{z}{H}\right)^2}{10}, & z \le H\\ 0, & z > H \end{cases}$$
 (5)

- and H = 500m denotes the prescribed boundary layer height.
- The governing equation (3) is numerically solved using the discretization strategies and physical configurations summarized in Table 1.
- Table 1. Configuration for idealized simulation

Horizontal grid	$\Delta x = 25 \text{km}, \ N_x = 101 \text{points} \ (L = 2500 \text{km})$
Vertical grid	$\Delta z = 10 \text{m}, \ N_z = 100 \ \text{levels} \ (z_{\text{top}} = 1000 \text{m})$
Initial conditions	$u_0(x, z) = 10 \text{ m s}^{-1} \text{ (horizontally and vertically uniform)}$
Lateral boundaries for	Periodic conditions: $u(x = 0) = u(x = L)$
advection	
Boundary conditions for	Surface friction velocity: $u_* = \begin{cases} 1.0, & x = L/2 \\ 0.01, & \text{elsewhere} \end{cases}$

vertical diffusion	Top: $\overline{u'w'}_{top} = 0$
Temporal discretization	Time-splitting with explicit advection $(\Delta t = 300 \text{ s})$ and fully
	implicit diffusion.
Spatial discretization	Advection: First-order upwind scheme
	Vertical diffusion: Second-order central difference

The surface friction configuration in Table 1 creates deliberate localized forcing, enabling controlled investigation of non-uniform surface effects on wind noise generation mechanisms in the simulated boundary layer flow.

Based on the configurations in Table 1, we conducted two contrasting idealized numerical experiments:

Ideal_Ctrl (Control Experiment):

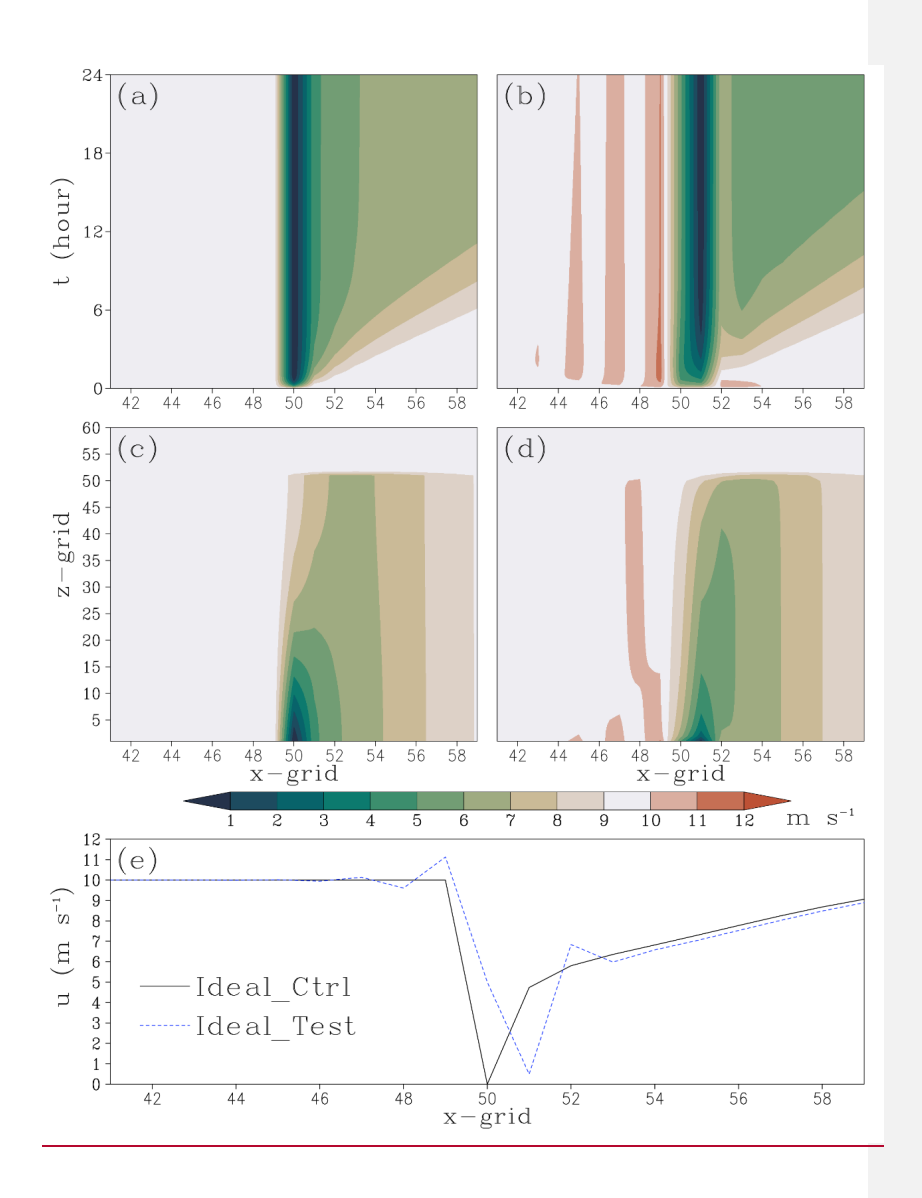
• Solves both horizontal advection and vertical diffusion terms at collocated grid points

Ideal_Test (Test Experiment):

- Solves horizontal advection at x_i
- Computes vertical diffusion at staggered grid points (x_i +Δx/2), with surface friction velocity (u_{*}) prescribed at corresponding staggered positions
- · Couples solutions through linear interpolation between grids

The two experiments are designed to isolate the impact of grid staggering on noise generation under inhomogeneous surface forcing. Both experiments are simulated for 24 hours (288 steps). Figure 7 displays the spatio-temporal distribution of the simulated u-wind from both cases. The Ideal_Ctrl simulation (Fig. 7a) exhibits localized wind reduction at the surface forcing site, with perturbations propagating downstream smoothly, demonstrating physically consistent behavior devoid of numerical noise. In contrast, the Ideal_Test simulation (Fig. 7b) shows that additional $2\Delta x$ grid-scale waves emerge near the local surface friction anomaly, superimposed on the expected frictional wind response. These $2\Delta x$ waves persist throughout the integration period with temporally quasi-constant amplitude, consistent with their behavior in CMA-GFS 3.0. Figure 7 (c-d) demonstrates that the influence of surface friction is confined to the boundary layer (below the 50th

model level). Compared Comparing Fig. 7 (d) with Fig. 7 (c), the staggered coupling generates $2\Delta x$ oscillation within the boundary layer at the point of non-uniform surface friction and these spurious noise patterns propagate to adjacent grid points, primarily near the surface. The 6-hour simulated lowest level u-wind (Fig. 7e) confirms that these $2\Delta x$ waves represent spurious numerical oscillations induced by dispersive energy propagation, which are most pronounced adjacent to the inhomogeneous surface forcing region. The Ideal_Test simulation results in Fig. 7 successfully reproduce both the distinctive $2\Delta x$ noise and their characteristic spatial distribution observed in CMA-GFS 3.0.



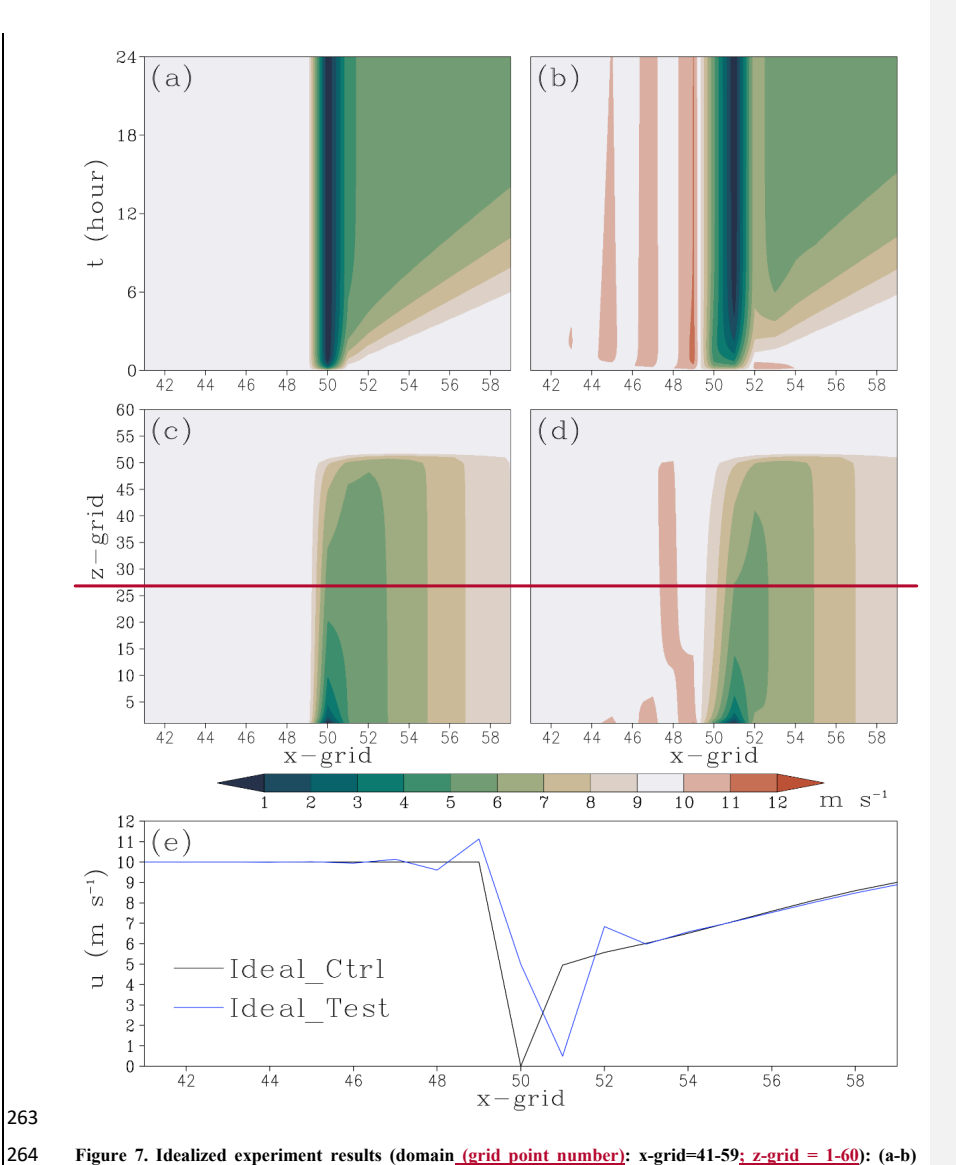


Figure 7. Idealized experiment results (domain_(grid point number): x-grid=41-59; z-grid = 1-60): (a-b) Temporal evolution of winds at the lowest model level in (a) Ideal_Ctrl and (b) Ideal_Test; (c-d) Vertical structure at 6 hour for (c) Ideal_Ctrl and (d) Ideal_Test; (e) 6-h wind at the lowest model level.

The idealized experiments reveal that the noise generation involves two coupled processes: (1) dispersive effects inherent to the advection-diffusion discretization (grid staggering), and (2) selective amplification and phase organization of small-scale components in surface forcing through these dispersive mechanismstests identify two primary noise sources: inconsistent advection-

diffusion grid staggering and inhomogeneous surface forcing. As demonstrated in Section 2.2, the stripe patterns in wind fields of CMA-GFS 3.0 predominantly occur over landmasses or near islands. This strongly indicates that wind stripe patterns in CMA-GFS 3.0 stem from inconsistent grid staggering in its dynamical-physical coupling. When combined with non-uniform surface forcing, this grid mismatch triggers dispersive wave propagation—ultimately producing the observed $2\Delta x$ stripe patterns.

3.4 Analysis of one-dimensional linear wave solution

For the one-dimensional linear damped wave equation:

$$\frac{\partial u}{\partial t} + c \frac{\partial u}{\partial x} = -\alpha u, \qquad \alpha > 0 \tag{6}$$

where c is the phase speed, $-\alpha u$ the damping term and α the damping coefficient, the analytic

280 solution takes the form:

$$u = u_n e^{-\alpha t} e^{ik(x - ct)} \tag{7}$$

281 Here k is the wavenumber. Eq. (7) describes an exact, non-dispersive wave propagation where all

282 wavenumbers propagate at identical phase speed c.

In Equation Eq. (6), the term $c \frac{\partial u}{\partial x}$ represents the advection term, while the damping term $-\alpha u$ acts as physical forcing. Based on the idealized experimental configuration outlined in the preceding section but with explicit damping time discretization, the right-hand side term of Eq. (6) can be discretized through two distinct numerical treatments. The first approach computes the damping term directly at the advection scheme's collocated grid points (x_i) , giving The numerical implementation employs a staggered grid configuration:—the advection term is discretized at the primary grid points (x), whereas the damping term is evaluated at half-grid offsets $(x \pm \Delta x/2)$ and then averaged—rather than being calculated directly at x. This arrangement transforms Eq. (6) into the following modified form:

$$\begin{split} \Delta u_{j}^{P} &= -\Delta t \alpha_{j} u_{j} \frac{\partial u(x)}{\partial t} + \epsilon \frac{\partial u(x)}{\partial x} \\ &= -\frac{\alpha \left(x - \frac{\Delta x}{2}\right) u \left(x - \frac{\Delta x}{2}\right) + \alpha \left(x + \frac{\Delta x}{2}\right) u \left(x + \frac{\Delta x}{2}\right)}{2} u \left(x + \frac{\Delta x}{2}\right)} \alpha > 0 \end{split} \tag{78}$$

where the subscript *j* represents the value at grid point *x_j*. Equation (8) corresponds to the

Ideal Ctrl configuration in the idealized experiment. This lead to the solution of Eq. (6) as Using

294 Taylor series expansion, the variable -u -at half grid offsets can be written as:

$$u_{j} = u_{j}^{D} e^{-\alpha t} \frac{1}{u} \left(x \pm \frac{\Delta x}{2} \right)$$

$$= u(x) \pm \frac{\partial u}{\partial x} \left(\frac{\Delta x}{2} + \frac{1}{2!} \frac{\partial^{2} u}{\partial x^{2}} \right) \left(\frac{\Delta x}{2} \right)^{2} \pm \frac{1}{3!} \frac{\partial^{3} u}{\partial x^{2}} \left(\frac{\Delta x}{2} \right)^{3} + O(\Delta x^{4})$$
(89)

- where $u_j^D = u_0 e^{ik(x_j c^D t)}$ is the wave solution of the advection term at x_j after spatiotemporal
- 296 <u>differencing. The specific form of phase velocity</u> c^D <u>depends on the finite difference scheme</u>
- 297 employed (Durran, 2010).
- 298 The alternative approach, analogous to the treatment in Eqs. (1) and (2), involves performing two
- 299 averaging operations during the physics-dynamic coupling, similar to the Ideal Test configuration.
- Consequently, the damping term in Eq. (6) leads to the following change in u at grid point x_i :

$$\Delta u_j^P = -\frac{\Delta t}{2} \left(\alpha_{j-\frac{1}{2}} \frac{u_{j-1} + u_j}{2} + \alpha_{j+\frac{1}{2}} \frac{u_j + u_{j+1}}{2} \right). \tag{9}$$

- 301 <u>For numerically resolved scales ($|k\Delta x| \ll 1$) where Taylor expansions remain valid, the variable u</u>
- 302 at neighboring grid points can be approximated as:

$$u_{j\pm 1} = u_j \pm \Delta x \frac{\partial u}{\partial x}\Big|_j + \frac{\Delta x^2}{2!} \frac{\partial^2 u}{\partial x^2}\Big|_i \pm \frac{\Delta x^3}{3!} \frac{\partial^3 u}{\partial x^3}\Big|_i + O(\Delta x^4), \tag{10}$$

- 303 where the notation $\frac{\partial u}{\partial x}$ denotes the partial derivatives of u at location x. Substituting Eq. (9) into
- 304 Eq. (8) and systematically neglecting fourth-order terms ($O(\Delta x^4)$), the analytical solution to Eq. (8)
- 305 becomes: where the notation $\frac{\partial u}{\partial x}\Big|_{i}$ denotes the partial derivatives of u at location x_{j} and $\Delta x =$
- 306 $x_{i+1} x_i$ is the Equidistant grid space. Substituting Eq. (10) into Eq. (9) and systematically
- neglecting fourth-order terms $(O(\Delta x^4))$, the individual wavelike solution to Eq. (6) becomes:

$$u_{j} = u_{j}^{D} e^{-\overline{\alpha}_{j}t} e^{-\frac{ik\Delta\alpha_{j}\Delta x}{4}t} e^{\frac{k^{2}\overline{\alpha}_{j}\Delta x^{2}}{4}t} e^{\frac{ik^{3}\Delta\alpha_{j}\Delta x^{3}}{4}t}, \mathbf{t}$$

$$= u_{j} e^{-\overline{\alpha}_{j}t} e^{-\frac{ik\Delta\alpha_{j}\Delta x}{4}t} e^{\frac{ik^{2}\overline{\alpha}_{j}\Delta x^{2}}{4}t}, \mathbf{t}$$

$$= u_{j} e^{-\overline{\alpha}_{j}t} e^{-\frac{ik\Delta\alpha_{j}\Delta x}{4}t} e^{\frac{ik^{2}\overline{\alpha}_{j}\Delta x^{2}}{4}t} e^{\frac{ik^{2}\overline{\alpha}_{j}\Delta x^{2}}{4}t}$$

$$= u_{j} e^{-\overline{\alpha}_{j}t} e^{-\frac{ik\Delta\alpha_{j}\Delta x}{4}t} e^{\frac{ik^{2}\overline{\alpha}_{j}\Delta x^{2}}{4}t} e^{\frac{ik^{2}\overline{\alpha}_{j}\Delta x^{2}}{4}t}$$

$$= u_{j} e^{-\overline{\alpha}_{j}t} e^{-\frac{ik\Delta\alpha_{j}\Delta x}{4}t} e^{\frac{ik^{2}\overline{\alpha}_{j}\Delta x^{2}}{4}t} e^{\frac{ik^{2}\overline{\alpha}_{j}\Delta x$$

- 308 where $\bar{\alpha}_j = \frac{\alpha_{j-\frac{1}{2}} + \alpha_{j+\frac{1}{2}}}{2}$, $\Delta \alpha_j = \alpha_{j+\frac{1}{2}} \alpha_{j-\frac{1}{2}}$. Compared to Eq. (8), Eq. (11) exhibits three additional
- 309 <u>terms in its wave solutions at x_i :</u>
- 310 where $\bar{\alpha} = \frac{\alpha(x + \frac{\Delta x}{2}) + \alpha(x \frac{\Delta x}{2})}{2}$, $\Delta \alpha = \frac{\alpha(x + \frac{\Delta x}{2}) \alpha(x \frac{\Delta x}{2})}{2}$. Eq. (10) exhibits three additional terms in its
- 311 wave solutions compare to Eq. (8)
- 312 l) The term $e^{-\frac{k\Delta\alpha_j\Delta_x}{4}t}e^{-\frac{k\Delta\alpha_d\Delta_x}{2}t}$ introduces a non-dispersive phase velocity modification.

- 313 2) The term $e^{\frac{k^2 \bar{a}_j \Delta x^2}{4} t} e^{\frac{k^2 a_i \Delta x^2}{8} t}$ enhances the wave amplitude (equivalently reducing damping).
- 314 3) The term $e^{i\frac{k^3\Delta\alpha_1\lambda x^3}{24}t}e^{i\frac{k^3\Delta\alpha_1\lambda x^3}{48}t}$ generates wavenumber-dependent phase modifications, a characteristic signature of dispersive wave propagation.
- 316 Compared to Eq. (7), tThe phase velocity in Eq. (11)(10) combines both non-dispersive and a
- 317 dispersive modifications to the phase velocity of advection c^D as $e^t = e + e^{-\frac{ik\hbar\alpha\Delta x}{2}t} +$
- 318 $\frac{k^2 \Delta \alpha \Delta x^2}{48} c' = c^D + \frac{\Delta \alpha_j \Delta x}{4} \frac{k^2 \Delta \alpha_j \Delta x^3}{24}.$
- When α exhibits no spatial variation (hence $\bar{\alpha} = \alpha$ and $\Delta \alpha_j \alpha = 0$), Eq. (11)(10) reduces to:

$$u_j = u_j^D e^{-\overline{\alpha}_j t} e^{\frac{k^2 \overline{\alpha}_j \Delta x^2}{4} t}, \frac{u = u_0 e^{-\alpha t} e^{\frac{ik(x - ct)}{8} e^{\frac{k^2 \alpha \Delta x^2}{8} t}}$$
 (1241)

- 320 where only the amplitude-modifying term persists, producing exclusively damping reduction
- 321 without any phase velocity modifications (neither non-dispersive shifts nor dispersive effects).
- Comparing Eqs. $\frac{-(7)(8)}{-(11)(10)}$ and $\frac{(12)(11)}{(11)}$ leads to the following conclusions:
- 1) The staggered-grid discretization scheme, where advection and damping terms are computed at offset grid points, fundamentally modifies wave solutions when compared to
- 325 collocated approaches.
- 326 2) For spatially varying damping coefficients (α), this numerical framework introduces
- 327 coupled amplitude-phase distortions, including wavenumber-dependent propagation speeds
- 328 characteristic of dispersive systems.
- 329 3) In contrast, uniform α fields restrict the influence of staggered-grid effects solely to
- amplitude modulation, preserving the original non-dispersive wave kinematics.
- 331 The reformulated Eq. (9) can be expressed as:

$$\Delta u_j^P = -\Delta t \bar{\alpha}_j u_j - \frac{\bar{\alpha}_j \Delta t}{4} \left(u_{j-1} - 2u_j + u_{j+1} \right) - \frac{\Delta \alpha_j \Delta t}{8} \left(u_{j+1} - u_{j-1} \right). \tag{13}$$

- 332 The right-hand side of Eq. (13) contains three distinct terms. The first term is identical to Eq. (7).
- 333 The second term exhibits the form of second-order horizontal diffusion note its negative coefficient,
- 334 which actually suppresses small-scale fluctuations in the damping process itself and clearly cannot
- generate $2\Delta x$ oscillations. This term corresponds to the amplitude modification term in Eq. (11),
- reducing the damping influence. The third term represents a second-order centered difference
- 337 scheme. As discussed by Durran (2010), second-order centered differencing introduces dispersion
- 338 in solutions to one-dimensional linear wave equations, producing upstream-propagating noise near

带格式的:缩进:首行缩进: 0 字符

spikes - precisely as demonstrated in our idealized experiments. Evidently, the noise source we 340 examine originates specifically from the third term of the right-hand side of Eq. (13).

339

341

342

343

344

345

346

347 348

349 350

351

352

Idealized experiments and linear wave analysis identify wind stripe noise in CMA-GFS 3.0 as requiring the coexistence of two independent factors: Physical forcing inhomogeneity (e.g., discontinuous non-uniform surface friction) and dynamics-physics-dynamics coupling on staggered grids. Critically, neither factor alone can generate dispersion noise-their combined presence is strictly necessary. This explains why stripes emerge preferentially over landmasses or near islands where sharp forcing gradients intersect with the model's inherent grid architecture (Fig. 2).

4. Confirming the origin of wind stripe patterns in CMA_GFS 3.0: sensitivity experiments

The preceding analysis demonstrates that low-level wind stripe noise over terrestrial region and near islands in CMA-GFS 3.0 stems from horizontal grid mismatch in physics-dynamics coupling. To validate this mechanism, we conduct a targeted sensitivity experiment (Exp_Test) by implementing conformal grid alignment for coupled processes.

In Fig. 1, the physical-point *u*-component can be expanded as $u_p\left(x+\frac{\Delta x}{2}\right)=u(x)+O(\Delta x)$. In 353

Exp_Test, we retain solely the zeroth-order approximation, enforcing $u_p u \left(x + \frac{\Delta x}{2}\right) = u(x)$. The 354

same treatment is applied to the v- component $(v_p \psi(y + \frac{\Delta y}{2}) = v(y))$, ensuring consistent 355

356 dynamics physics dynamics coupling for both horizontal velocity components. In correspondence

357 with Eqs. (1)-(2), we now present the modified formulations:

$$\begin{cases} P(u_{i,j}) = P\left(u_{i-\frac{1}{2}j}\right) \\ P(v_{i,j}) = P\left(v_{i,j-\frac{1}{2}j}\right) \end{cases}$$

$$(14)$$

When mapping from physics point back to the dynamics point, we have: 358

$$\begin{cases} \Delta u_{i-\frac{1}{2}j}^{P} = P(u_{i,j})\Delta t\\ \Delta v_{i,j-\frac{1}{2}}^{P} = P(v_{i,j})\Delta t \end{cases}$$

$$(15)$$

This conformal alignment ensures dynamical and physical processes are computed at coincident 359

360 grid points, eliminating the need for interpolation-based coupling shown in Eqs. (1)(1)-(2)(2). The

experimental configuration replicates the Exp_Ctrl setup described in Section 2.2, maintaining 361

带格式的:缩进:首行缩进: 0 字符

带格式的:缩进:首行缩进: 0 字符

20

identical initial conditions and physical parameterizations.

Compared to the results from Exp_Ctrl (Fig. 2), Exp_Test maintains small-scale variability in terrestrial wind fields while completely eliminating $2\Delta x$ stripe patterns (Fig. 8). The residual inhomogeneity over land, as evidenced in Fig. 8, reflects authentic physical responses to subgrid surface forcing inhomogeneity (e.g., topographic roughness, land-use variations), distinguishing it from numerical dispersion noise.

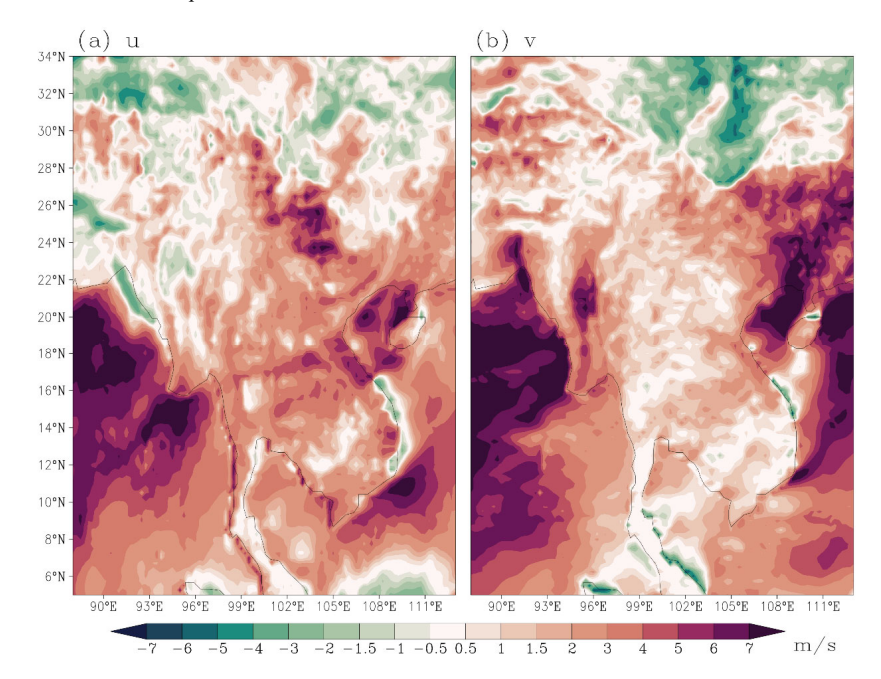


Figure 8 same as Fig. 2, but for Exp_Test.

Spectral analysis serves as a rigorous tool for quantifying energy distribution across frequencies. To diagnose the impacts of conformal dynamics-physics coupling on wind stripe patterns we conduct one-dimensional energy spectrum analysis separately for the u-component (zonal direction) and v-component (meridional direction). We selected the East Asian domain (70-145°E, 10-65°N) as a representative non-uniform surface region and the tropical Pacific (160°E-120°W, 20°S-20°N) as a typical uniform surface region for comparative analysis. The u- component was processed as a one-dimensional east-west oriented sequence for Fast Fourier Transform (FFT) analysis, while the v- component underwent identical treatment along the north-south axis. Through spectral analysis,

the power spectral density (PSD) was estimated by computing the squared modulus of the FFT coefficients (Fig. 9).

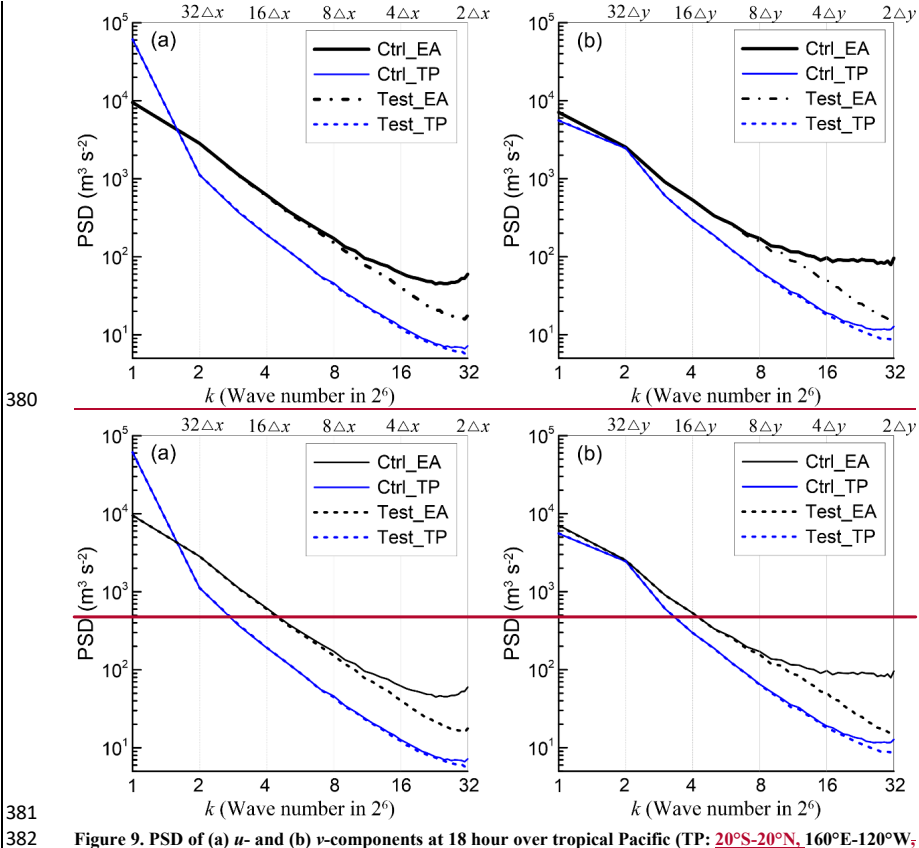


Figure 9. PSD of (a) u- and (b) v-components at 18 hour over tropical Pacific (TP: $20^{\circ}\text{S}-20^{\circ}\text{N}$, $160^{\circ}\text{E}-120^{\circ}\text{W}$, $160^{\circ}\text{E}-120^{\circ}\text{W}$, $160^{\circ}\text{E}-120^{\circ}\text{W}$, and East Asia (EA: $10^{\circ}-145^{\circ}\text{E}$, $10^{\circ}-65^{\circ}\text{N}$, $10^{\circ}-145^{\circ}\text{E}$) domains for Exp_Ctrl and Exp_Test.

The key results of PSD investigation can be summarized as follows:

383

384

385

386

387 388

389

390

391

- Over land, both u- and v- components in Exp_Ctrl demonstrate considerably strong energy
 at small scales (high wavenumbers), with no energy decay observed from 4Δx to 2Δx. In
 contrast, Exp_Test achieves significant suppression of small-scale energy, effectively
 mitigating high-frequency computational noise in terrestrial regions.
- 2) Over oceanic regions, the homogeneous ocean surfaces produce broadly similar spectral characteristics in both experiments. Although this general spectral agreement suggests that the horizontally homogeneous sea surface lacks the strong physical forcing inhomogeneity

required to generate prominent wind stripe patterns, minor differences can still be observed at the smallest resolved scale (2\Delta x). While most of the central Pacific study region features homogeneous oceanic surfaces, resolvable islands (e.g., Hawaii and numerous small islands east of Australia) introduce observable heterogeneity. As demonstrated in Fig. 10 (depicting near-surface winds over the eastern Australian waters), the Exp_Ctrl exhibits clear stripe patterns in low-level winds over some of the islands and their upwind regions, such as parts of Fiji (16-19°S, 177°-180°E) and Vanuatu (14-20°S, 166-171°E), whereas Exp_Test shows no such artifacts. This contrast highlights the role of surface inhomogeneity in noise generation the near surface wind power spectra exhibit remarkable consistency between Exp_Ctrl and Exp_Test. This spectral equivalence suggests that the horizontally homogeneous sea surface lacks the physical forcing inhomogeneity required to generate wind stripe patterns. The absence of surface inhomogeneity prevents the formation of computational noise in Exp_Ctrl, making Exp_Test's unstaggered dynamics physics coupling configuration exerts no significant impact in these regions.

 3) Terrestrial spectra exhibit distinct energy distributions between Exp_Ctrl and Exp_Test across scales ranging from $2\Delta x$ to $8\Delta x$. This spectral difference indicates that when inhomogeneous surface forcing combined with staggered-grid dynamic-physical coupling, dominant $2\Delta x$ -scale perturbations emerge consistently while statistically significant oscillations develop at discrete larger scales (e.g., $4\Delta x$).

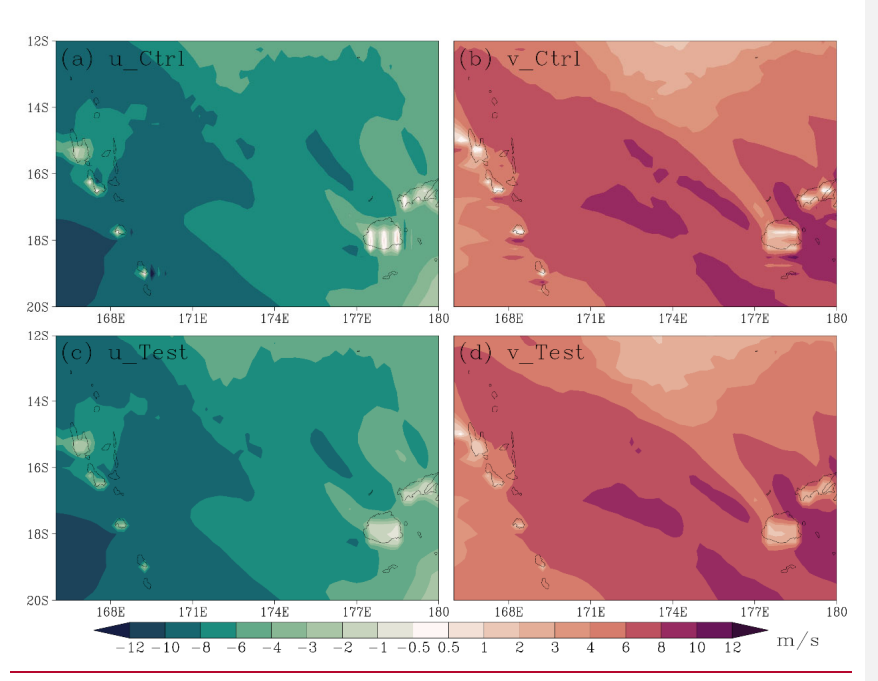


Figure 10. 18-hour forecasts of (a) u - and (b) v - component for Exp. Ctrl, and (c) u - and (d) v - component for Exp. Test, at the lowest model level from CMA - GFS 3.0.

Our sensitivity analysis confirms that the noise in CMA-GFS 3.0 originate specifically from the staggered-grid coupling between dynamic and physical processes over inhomogeneous surfaces. However, the noise-free Exp_Test configuration artificially decouples the wind field from mass fields (e.g., temperature and moisture) spatially in physical processes, violating fundamental physical constraints. We emphasize that Exp_Test serves solely as a mechanistic diagnostic to isolate the noise source rather than a viable approach for operational model improvement.

5. Conclusion and discussion

The removal of fourth-order horizontal diffusion in CMA-GFS 3.0 (Shen et al., 2023), while enhancing small-scale system simulations, has inadvertently exposed underlying $2\Delta x$ stripe patterns in low-level wind fields that were previously suppressed by the horizontal diffusion scheme. The results of a case study demonstrate that these stripe patterns exhibits one-dimensional oriented distribution characteristics, with meridional alignment in u-component and zonal alignment in v-component. These stripes maintain continuous presence throughout the 120-hour period, with

spatially predominant occurrence over land and near islands, while exhibiting diurnal amplitude modulation. We systematically elucidate the generation mechanism of these stripe patterns through a combination of numerical experiments and theoretical analysis.

Through controlled experiments with the dynamic core alone (no physics) and examination of associated surface static fields, we conclusively exclude the possibility that either the dynamic numerics or physical parameterizations independently generate the observed $2\Delta x$ noise. This leaves physics-dynamics coupling as the sole plausible origin, consistent with our previous findings (Chen et al., 2020) that $2\Delta x$ computational modes may emerge specifically when dynamics and physics interact through staggered-grid coupling. Two-dimensional idealized experiments successfully reproduced $2\Delta x$ waves generated at inhomogeneous surface friction points when combining advection and friction on staggered grids. Linear wave theory analysis further revealed that this dispersion effect originates from the coupling between dynamic advection and physical forcing on staggered grids under non-uniform physical forcing. These mechanistic analyses indicate that the grid mismatch in dynamic-physical coupling is the fundamental cause of noise generation over inhomogeneous surfaces.

Sensitivity experiments confirm that when dynamic-physical grid consistency is maintained and interpolation coupling is avoided, the wind field noise can be completely eliminated. Spectral analyses reveal land-ocean contrasts: Over oceans, staggered-grid coupling shows negligible impacts due to surface homogeneity. Over land, grid mismatch in physics-dynamics coupling under inhomogeneous surface elevates small-scale energy $(2\Delta x-8\Delta x)$, generating broadband noise, while unstaggered physics-dynamics coupling restores the energy spectrum to a reasonable decay curve with decreasing scale.

Our results demonstrate that the stripe noise in low-level wind field of CMA-GFS 3.0 stems from grid mismatch in physics-dynamics coupling under non-uniform forcing conditions. These findings offer critical insights for other NWP models employing similar grid configurations, revealing potential numerical dispersion risks in physical-dynamics coupling on traditional staggered grids.

Building on these findings, we systematically evaluate potential solutions to mitigate wind-field noise in CMA-GFS 3.0. Since surface inhomogeneity is inherently present in NWP models, one essential approach to noise reduction involves resolving the grid mismatch between physics

parameterizations and dynamical core. In latitude-longitude grid configurations, the Arakawa C-grid exhibits superior dispersion characteristics compared to unstaggered A-grid arrangements, particularly in maintaining proper phase relationships for geostrophic adjustment processes. However, adopting an A-grid configuration may introduce computational challenges in the dynamical core that could degrade numerical accuracy.

It must be emphasized that grid configuration represents a fundamental architectural feature of numerical modeling systems. As the cornerstone of model design, grid setup is determined at the earliest development stage. Redesigning grids equates to building an entirely new model system, making modifications to CMA-GFS's existing Arakawa C-grid configuration unfeasible. An alternative approach would involve computing wind fields directly on the dynamics grid within physical parameterizations. However, this strategy encounters substantial technical obstacles owing to the inherently tight coupling between wind and temperature/moisture fields in physical processes, especially when managing their interactions on staggered grids. Consequently, this method also proves extremely difficult to implement in CMA-GFS.

A compromise solution involves employing higher-order horizontal diffusion or filtering which is widely implemented in NWP models. Methods like high-order horizontal diffusion can effectively eliminate $2\Delta x$ high-frequency noise while retaining most resolvable-scale energy. Specifically, as demonstrated by Xue (2000), 4th-order horizontal diffusion preserves about 80% of $4\Delta x$ -scale spectral energy, and 6th-order diffusion achieves ~90% retention at this scale. However, one-dimensional linear wave analysis shows that staggered grid coupling under non-uniform forcing not only produces dispersion effects but also alters wave amplitude and phase speed, and these systematic deviations cannot be corrected by simple noise-removal tools.

Higher-order horizontal diffusion can serve as a practical remedy for unexplained noise. However, this study has definitively pinpointed the specific sources of wind-field noise in CMA-GFS. We therefore propose the following targeted Based on the conclusions of this study and the above discussion, we propose two recommendations:

While the piecewise-constant sampling method (Eqs. (15) and (16)) effectively suppresses
 numerical noise, it may introduce directional biases. A more physically consistent approach
 would be upwind sampling, where: For the current CMA GFS system, we recommend implementing high-order horizontal diffusion or similar treatment methods globally to

eliminate low level wind field noise, and systematically evaluating its impact on forecasts;

$$\begin{cases} u_p\left(x + \frac{\Delta x}{2}\right) = u(x) & \text{if } u \ge 0 \\ u_p\left(x + \frac{\Delta x}{2}\right) = u(x + \Delta x) & \text{otherswise} \end{cases}$$
 (17)

This straightforward approach offers immediate operational feasibility and can be rapidly implemented to address the issue. We recommend trial implementation in the operational system followed by comprehensive impact assessment.

带格式的: 正文,缩进: 左侧: 0 厘米,悬挂缩进: 3.37 字符,首行缩进: -3.37 字符, 无项目符号或编 号

带格式的:字体: (默认) Times New Roman

- 4.2. The strong connection between wind and heat transfer in the boundary layer turbulent diffusion makes it difficult to compute momentum diffusion directly at wind grid points.

 As demonstrated in Chen et al. (2020), interpolating the diffusivity (rather than prognostic variables) effectively eliminated vertical grid-scale noise in thermodynamic fields a numerical artifact originally induced by staggered-grid coupling between dynamic and physical processes. Following this approach, we recommend averaging the diffusion coefficient back to the wind points and performing the vertical diffusion on the wind points, thereby avoiding interpolation of prognostic wind variables. Given its demonstrated efficacy in addressing similar discretization challenges in our previous studies (Chen et al., 2020), this approach merits implementation and systematic evaluation.
- 2-3. In developing next-generation model frameworks, the coordination of dynamic-physical coupling should be a core design consideration to fundamentally prevent such issues.

Data and code availability. The CMA-GFS 3.0 operational system code is proprietary to the China Meteorological Administration and cannot be publicly released. For inquiries about the model framework, contact the operational management department of CEMC or the author, Jiong Chen (ejiong@ema.gov.en), for further assistancehas been archived at https://doi.org/10.5281/zenodo.16516966 (Chen, 2025). The idealized test code for diagnosing stripe patterns, along with all analysis scripts and data used to generate the figures, is available at https://doi.org/10.5281/zenodo.15597504 (Chen et al., 2025).

Author contributions. JC conducted the model simulations, designed the idealized experiments,

514	performed the diagnostic analysis, and wrote the manuscript. YS first identified the stripe patterns
515	in operational forecasts and excluded the dynamical core's contribution through controlled
516	numerical tests. All other authors participated in result interpretation, provided critical feedback
517	during manuscript revisions, and contributed to figure improvements.
518	
519	Competing interests. The contact author has declared that none of the authors has any competing
520	interests.
521	
522	Acknowledgements. This research was supported by the NSFC Major Project (42090032) and
523	Beijing Natural Science Foundation for Young Scholars (8254056).
524	
525	References
526	Arakawa, A.: Computational design for long-term numerical integration of the equations of fluid
527	motion: Two dimensional incompressible flow. Part I. J. Comput. Phys., 1, 119-143,
528	https://doi.org/10.1016/0021-9991(66)90015-5, 1966.
529	Arakawa, A., & Lamb, V. R.: Computational design of the basic dynamical processes of the UCLA
530	general circulation model, General circulation models of the atmosphere, 17 (Supplement C),
531	173–265, https://doi.org/10.1016/B978-0-12-460817-7.50009-4, 1977.
532	Batteen, M. L. and Han, YJ.: On the computational noise of finite-difference schemes used in ocean
533	models, Tellus, 33, 387-396, https://doi.org/10.1111/j.2153-3490.1981.tb01761.x, 1981.
534	Bauer, P., Thorpe, A, and Brunet, G.: The quiet revolution of numerical weather prediction, <i>Nature</i> ,
535	525, 47-55, http://dx.doi.org/10.1038/nature14956 , 2015.
536	Beljaars, A., Brown A., and Wood, N.: A new parameterization of turbulent orographic form drag,
537	Q. J. R. Meteorol. Soc., 130, 1327–1347, https://doi.org/10.1256/qj.03.73, 2004.
538	Blackadar, A. K.: Boundary layer wind maxima and their significance for the growth of nocturnal
539	inversions, Bull. Amer. Meteor. Soc., 38, 283-290, https://doi.org/10.1175/1520-0477-38.5.283,
540	1957.
541	Charney I.G. and Phillips N.A.: Numerical integration of the quasi-geostrophic equations for

- barotropic and simple baroclinic flows, Journal of Meteorology, 10, 71-99,
- 543 <u>https://doi.org/10.1175/1520-0469(1953)010<0071:NIOTQG>2.0.CO;2</u>, 1953.
- 544 Chen, D. H., Xue, J. S., Yang, X. S., Zhang, H. L., Shen, X. S., Hu, J., L., Wang, Y., Ji, L. R. and
- 545 Chen, J. B.: New generation of multi-scale NWP system (GRAPES): general scientific design.
- 546 Chinese Science Bulletin, 52, 3433-3445, https://doi.org/10.1007/s11434-008-0494-z, 2008.
- 547 Chen, G., I. M. Held, and Robinson, W. A.: Sensitivity of the latitude of the surface westerlies to
- surface friction, *J. Atmos. Sci.*, 64, 2899–2915, https://doi.org/10.1175/JAS3995.1, 2007.
- 549 Chen, J.: CMA-GFS 3.0 code egusphere-2025-2704, Zenodo [code],
- 550 https://doi.org/10.5281/zenodo.16516966, 2025.
- 551 Chen, J., Ma, Z. S. and Su, Y.: Boundary layer coupling to Charney-Phillips vertical grid in
- 552 GRAPES model (in Chinese). J. Appl. Meteor. Sci., 28, 52–60, https://doi.org/10.11898/1001-
- 553 7313.20170105, 2017.
- 554 Chen, J., Ma, Z. S., Li, Z., Shen, X. S., Su, Y., Chen, Q. Y. and Liu, Y. Z.: Vertical diffusion and
- cloud scheme coupling to the Charney-Phillips vertical grid in GRAPES global forecast system,
- 556 *Quart. J. Roy. Meteor. Soc.*, 146, 2191–2204, https://doi.org/10.1002/qj.3787, 2020.
- 557 Chen, J., Su, Y., Li, Z., Ma, Z. S. and Shen, X. S.: Replication data: Stripe Patterns in Wind Forecasts
- Induced by Physics-Dynamics Coupling on a Staggered Grid in CMA-GFS 3.0, Zenodo [data
- set], https://doi.org/10.5281/zenodo.15597504, 2025.
- 560 Chen, Q. Y., Shen, X. S., Sun, J. and Liu K.: Momentum budget diagnosis and the parameterization
- of subgrid-scale orographic drag in global GRAPES, J. Meteor. Res., 30, 771-788,
- 562 <u>https://doi.org/10.1007/s13351-016-6033-y</u>, 2016.
- 563 Côté, J., Gravel, S., Méthot, A., Patoine, A., Roch, M. and Staniforth, A.: The operational CMC-
- MRB Global Environmental Multiscale (GEM) model. Part I: Design considerations and
- 565 formulation, Mon. Wea. Rev., 126, 1373-1395, https://doi.org/10.1175/1520-
- 566 <u>0493(1998)126%3C1373:TOCMGE%3E2.0.CO;2</u>, 1998.
- 567 Dai, Y. J., Zeng, X. B., Dickinson, R. E., Baker, I., Bonan, G. B., Bosilovich, M. G., Denning, A. S.,
- Dirmeyer, P. A., Houser, P. R., Niu, G. Y., Oleson, K. W., Schlosser, C. A. and Yang, Z-L.: The
- 569 common land model. Bull. Amer. Meteor. Soc., 84, 1013–1023, https://doi.org/10.1175/BAMS-
- 570 <u>84-8-1013</u>, 2003.
- 571 Durran, D. R.: Numerical Methods for Fluid Dynamics: With Applications to Geophysics (2nd ed.).

- 572 Springer. DOI: https://link.springer.com/book/10.1007/978-1-4419-6412-0, 2010.
- 573 Gross, M., Malardel, S., Jablonowski, C. and Wood, N.: Bridging the (knowledge) gap between
- physics and dynamics. Bull. Amer. Meteor. Soc., 97, 137–142, https://doi.org/10.1175/BAMS-
- 575 <u>D-15-00103.1</u>, 2016.
- 576 Gross, M., Wan, H., Rasch, P. J., Caldwell, P. M., Williamson, D. L., Klocke, D., Jablonowski, C.,
- 577 Thatcher, D. R., Wood, N., Cullen, M., Beare, B., Willett, M., Lemarié, F., Blayo, E., Malardel,
- 578 S., Termonia, P., Gassmann, A., Lauritzen, P. H., Johansen, H., Zarzycki, C. M., Sakaguchi, K.
- and Leung, R.: Physics-dynamics coupling in weather, climate, and Earth system models:
- 580 Challenges and recent progress. Mon. Wea. Rev., 146, 3505-3544,
- 581 <u>https://doi.org/10.1175/MWR-D-17-0345.1</u>, 2018.
- 582 Han, J., and Pan, H.-L.: Revision of convection and vertical diffusion schemes in the NCEP global
- forecast system. Wea. Forecasting, 26, 520–533, https://doi.org/10.1175/WAF-D-10-05038.1,
- 584 2011.
- 585 Hersbach, H., Bell, B., Berrisford, P., Hirahara, S., Horányi, A., Muñoz-Sabater, J., Nicolas, J.,
- Peubey, C., Radu, R., Schepers, D., Simmons, A., Soci, C., Abdalla, S., Abellan, X., Balsamo,
- 587 G., Bechtold, P., Biavati, G., Bidlot, J., Bonavita, M., De Chiara, G., Dahlgren, P., Dee, D.,
- Diamantakis, M., Dragani, R., Flemming, J., Forbes, R., Fuentes, M., Geer, A., Haimberger, L.,
- Healy, S., Hogan, R. J., Hólm, E., Janisková, M., Keeley, S., Laloyaux, P., Lopez, P., Lupu, C.,
- 590 Radnoti, G., de Rosnay, P., Rozum, I., Vamborg, F., Villaume, S., and Thépaut, J.-N.: The ERA5
- 591 Global Reanalysis, Q. J. Roy. Meteor. Soc., 146, 1999–2049, https://doi.org/10.1002/qj.3803,
- 592 2020.
- 593 Kim, Y.-J., Eckermann, S. D. and Chun, H.-Y.: An overview of the past, present and future of
- 594 gravity-wave drag parameterization for numerical climate and weather prediction models.
- 595 *Atmos-Ocean*, 41, 65–98, https://doi.org/10.3137/ao.410105, 2003.
- 596 Kim, Y.-J. and Doyle, J. D.: Extension of an orographic-drag parametrization scheme to incorporate
- 597 orographic anisotropy and flow blocking, Q. J. R. Meteorol. Soc., 131, 1893-1921,
- 598 https://doi.org/10.1256/qj.04.160, 2005.
- 599 Lorenz, E.N.: Energy and numerical weather prediction, Tellus, 12, 364-373,
- 600 https://doi.org/10.1111/j.2153-3490.1960.tb01323.x, 1960.
- 601 Ma, Z. S., Liu, Q. J., Zhao, C. F., Shen, X. S., Wang, Y., Jiang, J. H., Li, Z. and Yung, Y.: Application

- and evaluation of an explicit prognostic cloud-cover scheme in GRAPES global forecast system.
- 603 J. Adv. Model. Earth Syst., 10, 652–667, https://doi.org/10.1002/2017MS001234, 2018.
- 604 Mesinger, F. and Arakawa, A.: Numerical methods used in atmospheric models, Report, Global
- Atmospheric Research Programme (GARP), https://oceanrep.geomar.de/id/eprint/40278/ (last
- 606 access: 3 June 2025), 1976.
- 607 McFarlane N. A.: The effect of orographically excited gravity wave drag on the general circulation
- of the lower stratosphere and troposphere, J. Atmos. Sci., 44, 1775-1800,
- 609 https://doi.org/10.1175/1520-0469(1987)044<1775:TEOOEG>2.0.CO;2, 1987.
- 610 Morcrette, J.-J., Barker, H. W., Cole, J. N. S., Iacono, M. J. and Pincus, R.: Impact of a new radiation
- package, McRad, in the ECMWF Integrated Forecast System, Mon. Wea. Rev., 136, 4773–4798,
- 612 https://doi.org/10.1175/2008MWR2363.1, 2008.
- Pincus, R., Barker, H. W. and Morcrette, J.-J.: A fast, flexible, approximate technique for computing
- 614 radiative transfer in inhomogeneous cloud fields. J. Geophys. Res., 108, 4376,
- 615 https://doi.org/10.1029/2002JD003322, 2003.
- Randall, D. A.: Geostrophic adjustment and the finite-difference shallow-water equations, Mon.
- 617 Weather Rev., 122, 1371–1377, https://doi.org/10.1175/1520-
- 618 <u>0493(1994)122<1371:GAATFD>2.0.CO;2, 1994.</u>
- Raymond, W. H. and Garder, A.: A spatial filter for use in finite area calculations, Mon. Weather
- 620 Rev., 116, 209-222, https://doi.org/10.1175/1520-
- 621 <u>0493(1988)116%3C0209:ASFFUI%3E2.0.CO;2</u>, 1988.
- 622 Robinson, W. A.: Dissipation dependence of the jet latitude, J. Clim., 10, 176-182,
- 623 https://doi.org/10.1175/1520-0442(1997)010<0176:DDOTJL>2.0.CO;2, 1997.
- 624 Sela, J. G.: The derivation of sigma-pressure hybrid coordinate semi-Lagrangian model equations
- for the NCEP Global Forecast System, NOAA Technical Report NWS 34, National Centers for
- Environmental Prediction, https://repository.library.noaa.gov/view/noaa/6971 (last access: 3
- 627 June 2025), 2010.
- 628 Shapiro R.: Smoothing, filter, and boundary effect. Review of Geophysics and Space Physics, 8,
- 629 359-387, https://doi.org/10.1029/RG008i002p00359, 1970.
- 630 Shapiro R.: Linear filtering, *Math. Comp.*, 29: 1094-1097, http://dx.doi.org/10.2307/2005747, 1975.
- 631 Skamarock, W. C. and Klemp, J. B.: A time-split nonhydrostatic atmospheric model for weather

- research and forecasting applications, J. Comput. Phys, 227, 3465-3485,
- 633 <u>https://doi.org/10.1016/j.jcp.2007.01.037</u>, 2008.
- 634 Stull, R. B.: An introduction to Boundary layer Meteorology, Kluwer Academic Publishers.
- 635 <u>https://link.springer.com/book/10.1007/978-94-009-3027-8</u>, 1988.
- 636 Sandu, I., Bechtold, P., Beljaars, A., Bozzo, A., Pithan, F., Shepherd, T. G. and Zadra, A.: Impacts
- 637 of parameterized orographic drag on the Northern Hemisphere winter circulation, J. Adv. Model.
- 638 Earth Syst., 8, 196–211, https://doi.org/10.1002/2015MS000564, 2016.
- 639 Shen, X. S., Wang, J. J., Li, Z. C., Chen, D. H. and Gong J. D: Research and Operational
- Development of Numerical Weather Prediction in China, J. Meteor. Res., 34, 675-698,
- 641 https://doi.org/10.1007/s13351-020-9847-6, 2020.
- 642 Shen, X. S., Su, Y., Zhang, H. L. and Hu, J. L.: New Version of the CMA-GFS Dynamical Core
- Based on the Predictor-Corrector Time Integration Scheme, J. Meteor. Res., 37, 273-285,
- 644 <u>https://doi.org/10.1007/s13351-023-3002-0</u>, 2023.
- 645 Walters, D., Boutle, I., Brooks, M., Melvin, T., Stratton, R., Vosper, S., Wells, H., Williams, K.,
- Wood, N., Allen, T., Bushell, A., Copsey, D., Earnshaw, P., Edwards, J., Gross, M., Hardiman,
- 647 S., Harris, C., Heming, J., Klingaman, N., Levine, R., Manners, J., Martin, G., Milton, S.,
- Mittermaier, M., Morcrette, C., Riddick, T., Roberts, M., Sanchez, C., Selwood, P., Stirling, A.,
- Smith, C., Suri, D., Tennant, W., Vidale, P. L., Wilkinson, J., Willett, M., Woolnough, S., and
- Xavier, P.: The Met Office Unified Model Global Atmosphere 6.0/6.1 and JULES Global Land
- 6.0/6.1 configurations, Geosci. Model Dev., 10, 1487–1520, https://doi.org/10.5194/gmd-10-
- 652 <u>1487-2017</u>, 2017.
- Wang, G. H., Chen, F. F., Shen, X., S. and Hu, J., L.: The impact of topography filter processing and
- horizontal diffusion on precipitation prediction in numerical model, Chinese J. Geophys. (in
- 655 Chinese), 51, 1642-1650, https://doi.org/10.3321/j.issn:0001-5733.2008.06.003, 2008.
- Wurtele, M. G.: On the problem of truncation error, Tellus, 13, 379-391,
- 657 https://doi.org/10.3402/tellusa.v13i3.9514, 1961.
- 658 Xu, W., and Lin, C. A.: A numerical solution of the linear Rayleigh Bernard convection equations
- 659 with B- and C-grid formulations, Tellus, 45, 193-200,
- https://doi.org/10.3402/tellusa.v45i3.14869, 1993.
- Kue, M.: High-order monotonic numerical diffusion and smoothing, Mon. Weather Rev., 128, 2853-

 $2864, \underline{https://doi.org/10.1175/1520-0493(2000)128\%3C2853: HOMNDA\%3E2.0.CO; 2, 2000.$